Imaging the dopamine transporter: Varrone and Halldin provide an overview of the most commonly used SPECT and PET radioligands for dopamine transporter imaging and review current applications in neurologic and psychiatric disorders. . . . . ***Page 1331***

Imaging β-cell mass: Bormans comments on challenges in noninvasive quantification of β-cell mass and previews an article in this issue of *JNM* on ^{11}C-dihydrotetrabenazine, a PET tracer with promise for longitudinal assessment in therapies for diabetes. . . . . ***Page 1335***

PET and prognosis in chemotherapy: Cerci and colleagues assess the prognostic value of ^{18}F-FDG PET after 2 cycles of chemotherapy in patients with early and advanced Hodgkin lymphoma, including those classified as at high and low risk. . . . . ***Page 1337***

Erlotinib response monitoring with PET: Aukema and colleagues evaluate the role of integrated ^{18}F-FDG PET/CT in early identification of response to an epidermal growth factor receptor tyrosine kinase inhibitor in non–small cell lung cancer. . . . . ***Page 1344***

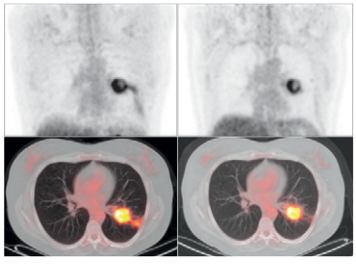

Response prediction in NETs: Haug and colleagues investigate the utility of ^{68}Ga-DOTATATE PET/CT for early prediction of progression and clinical outcomes after a first cycle of peptide receptor radionuclide treatment in patients with well-differentiated neuroendocrine tumors. . . . . ***Page 1349***

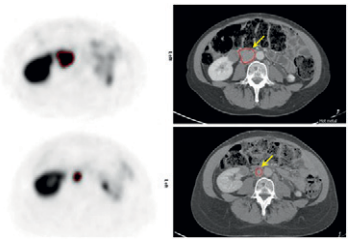

Aortic inflammation in COPD: Coulson and colleagues use ^{18}F-FDG PET to assess vascular inflammation in patients with chronic obstructive pulmonary disease to elucidate the mechanisms of increased risk of cardiovascular disease in this cohort. . . . . ***Page 1357***

Posttherapy SPECT/CT in thyroid cancer: Grewal and colleagues explore whether ^{131}I SPECT/CT changes the need for additional cross-sectional imaging after ^{131}I therapy in patients with different types of thyroid carcinoma or modifies conventional thyroid risk-of-recurrence classifications. . . . . ***Page 1361***

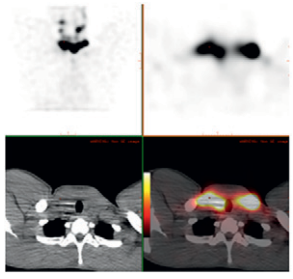

PET volume reproducibility: Hatt and colleagues establish the repeatability and reproducibility limits of several volume-related ^{18}F-FDG and ^{18}F-FLT PET image–derived indices commonly used in clinical practice. . . . . ***Page 1368***

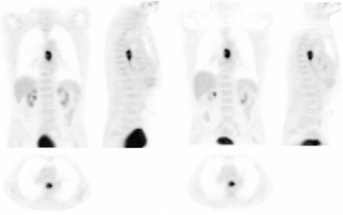

Efficacy and toxicity after ^{90}Y spheres: Strigari and colleagues implement radiobiologic models for tumor control and normal-tissue complication probabilities to describe more effectively local response and liver toxicity rates in ^{90}Y-sphere selective internal radiation therapy in nonresectable hepatocellular carcinoma. . . . . ***Page 1377***

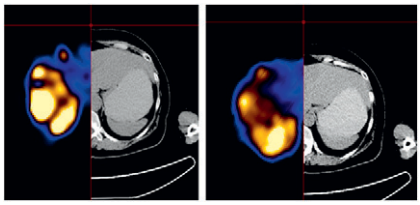

^{18}F-FAZA modeling: Shi and colleagues report on a feasibility study to assess hypoxia kinetic models using voxelwise cross-analysis between uptake of the perfusion tracer ^{15}O-H_2O and the hypoxia tracer ^{18}F-fluoroazomycin arabinoside. . . . . ***Page 1386***

New human reporter gene: Likar and colleagues describe a series of human-derived, pyrimidine-specific reporter genes based on human deoxycytidine kinase and suitable for clinical PET during treatment with acycloguanosine-based cytotoxic drugs. . . . . ***Page 1395***

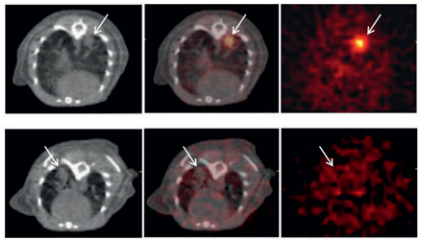

Neuroinflammation in subcortical stroke: Thiel and colleagues use diffusion tensor image–guided ^{11}C-PK11195 PET

to identify activated microglia in vivo after stroke in a longitudinal study investigating temporal dynamics and relating microglial activity to pyramidal tract damage. . . . . ***Page 1404***

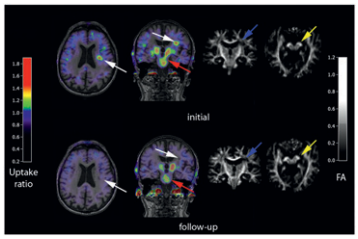

CB1 PET in Huntington disease: Van Laere and colleagues measure type 1 cannabinoid receptor, a crucial modulator of synaptic transmission, in the brains of patients with Huntington disease and healthy controls. . . . . ***Page 1413***

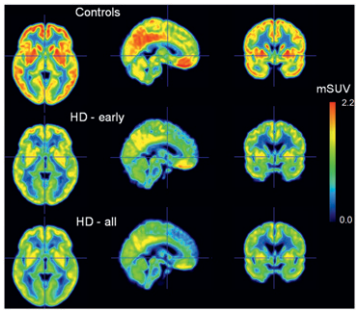

Probes for dementia: Kadir and Nordberg provide an educational overview of imaging techniques in neurodegenerative disorders causing dementia, including Alzheimer disease, frontotemporal dementia, dementia with Lewy bodies, and dementia in Parkinson disease.***Page 1418***

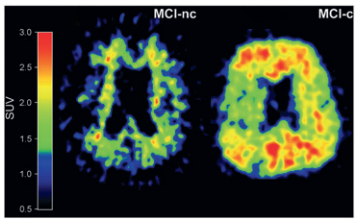

MR-based attenuation correction: Catana and colleagues address attenuation correction challenges in combined PET/MRI and introduce a method based on MRI data from a single dedicated sequence, with utility in a PET/MRI human brain scanner prototype.. . . . . ***Page 1431***

^{11}C-DTBZ binding in pancreas: Fagerholm and colleagues assess the islet and vesicular monoamine transporter 2 specificity of ^{11}C-dihydrotetrabenazine and describe its potential in PET imaging of pancreatic β-cell mass in type 1 diabetes. . . . . ***Page 1439***

^{18}F-FLT PET in ENT1-knockout mice: Paproski and colleagues determine whether equilibrative nucleoside transporter 1 is important for ^{18}F-FLT uptake in normal tissues and tumors. . ***Page 1447***

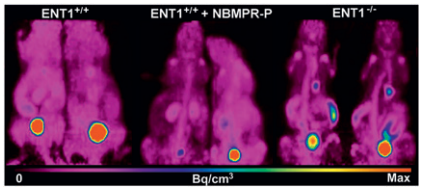

Multimodality imaging of SSTR2: Chen and colleagues report on the development of a somatostatin receptor–enhanced green fluorescent protein fusion construct for nuclear and fluorescent multimodality imaging. . . . . ***Page 1456***

PET-based nucleoside tracer transport: Plotnik and colleagues examine the relative roles of different nucleoside PET transport mechanisms on uptake and retention of thymidine, fluorothymidine, and FMAU. . . . . ***Page 1464***

^{76}Br-MBBG PET for tumor imaging: Watanabe and colleagues label *meta*-bromobenzylguanidine with ^{76}Br, a positron emitter, and evaluate its potential as a PET tracer in norepinephrine transporter–expressing tumors. . . . . ***Page 1472***

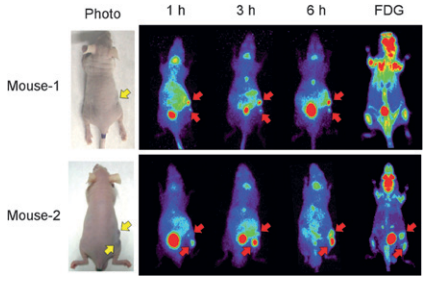

Biodistribution/dosimetry of ^{18}F-AV-133: Lin and colleagues investigate the biodistribution and radiation dosimetry of a potential vesicular monoamine transporter 2 imaging agent, with encouraging results in humans. . . . . ***Page 1480***

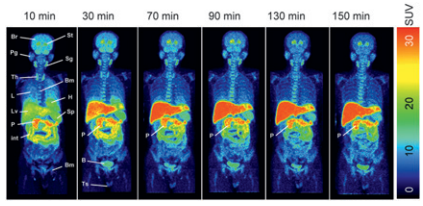

ON THE COVER

Preliminary results suggest that a new MRI-based attenuation correction method may be as accurate as the segmented CT method and applicable to quantitative neurologic PET/MRI studies. Selection of the linear attenuation coefficient for bone affects PET data quantification, as shown in these representative images of relative changes for 3 attenuation correction models.

See page 1434.